

# From Monolayers to Bilayers: Mesostructural Evolution in DDAB/Water/Tetradecane Microemulsions

Maurizio Olla,<sup>†</sup> Armin Semmler,<sup>‡</sup> Maura Monduzzi,<sup>§</sup> and Stephen T. Hyde<sup>\*,||</sup>

*Dipartimento Chimica Inorganica ed Analitica, Università di Cagliari, and Dipartimento Scienze Chimiche, CSGI-Università di Cagliari, Cittadella Universitaria S.S. 554 bivio Sestu, Monserrato, 09042 (CA), Italy, Infineon Ventures GmbH, St.-Martin-Strasse 53, 81541 München, Germany, and Applied Maths Department, Research School of Physical Sciences, Australian National University, Canberra ACT 0200, Australia*

*Received: December 22, 2003; In Final Form: April 18, 2004*

Small-angle X-ray (SAXS) scattering and  $^{14}\text{N}$  NMR relaxation were determined for microemulsion samples formed from didodecyl dimethylammonium bromide (DDAB), water, and tetradecane to deduce the associated microstructures. The swelling features within the tetradecane microemulsion are unusual compared with those of DDAB/water/alkane analogues formed with shorter *n*-alkanes: tetradecane-containing microemulsions do not show the characteristic anti-percolation transition seen for the latter microemulsions. Experimental data along tetradecane dilution lines are consistent with a continuous transition from a bilayer to monolayer structure of the surfactant interface. The evolution is topologically complex. It involves the annealing of bilayer punctures that occur on oil dilution. A quantitative model that allows continuous transformation from multihanded bilayers (typical of  $L_3$  sponge mesophases) to multihanded monolayers (typical of microemulsions modeled with shorter chained alkanes) is proposed that well fits the observed behavior.

## 1. Introduction

Ternary mixtures of water and hydrocarbons with the double-chained cationic quaternary ammonium surfactant didodecyl dimethylammonium bromide (DDAB) have yielded a wealth of data on microstructure in both their liquid-crystalline<sup>1,2</sup> and microemulsion mesophases.<sup>3–22</sup>

The topology and geometry of surfactant self-assemblies in many such phases are well accounted for by invoking fixed local curvature at the oil–water interface and global packing constraints. Local interfacial curvature, described by an effective surfactant parameter, is set for the DDAB systems by the energetics of oil adsorption into the surfactant tails.<sup>23</sup> The antipercolation behavior seen in ternary DDAB/water/alkane mixtures, with cyclohexane, alkenes, and alkanes up to dodecane, emerges as a simple consequence of global packing constraints at constant interfacial curvature.<sup>10</sup> This demands a continuous decrease in the connectivity of the water channels on water dilution.<sup>5,7,21,22</sup>

For these alkane/water/DDAB microemulsions, a simple model reminiscent of connected water channels approximates the microstructure quantitatively.<sup>12,24–26,28</sup> This so-called “DOC cylinder” model approximates that mesostructure as follows. First, a geometrically random distribution of sites in space ( $x$ ,  $y$ ,  $z$ ) is selected. Voronoi cells are constructed about each site; these sites are then decorated by spheres, interconnected by cylinders passing through a surface of the faces of Voronoi cells. The resulting structure is interconnected (percolated) and hyperbolic for connectivity  $z > 1.5$  and consists of disconnected spheres for  $z = 0$  (Figure 1). For a certain composition DDAB/

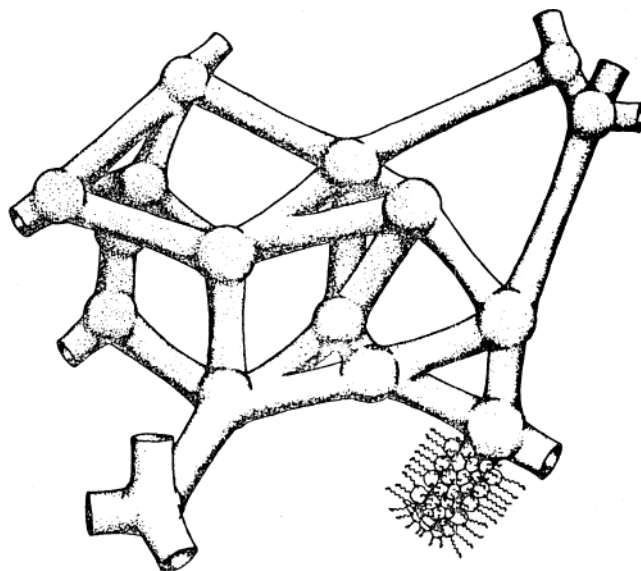


**Figure 1.** Cartoon view of the monolayer geometry and topology for bicontinuous (type 2) microemulsions according to the DOC cylinders model. The interconnected tubes enclose the polar domains of the aggregate (water plus ionic headgroups). The hydrophobic chains are indicated by zig-zag lines sheathing the oil–water interface in the lower left-hand part of the picture.

water/oil ( $s/w/o$ ), that surface(s) geometry is set by  $z$  and the spheres' and cylinders' radii to accommodate the hydrophilic volume fractions that lie on either side of the surface. To constrain the structure filling at a certain  $s/w/o$  ratio,  $z$  is selected to accommodate a preferred value of the surfactant parameter.

The concept of a surfactant parameter can be generalized<sup>27</sup> to describe the domains on both sides of any homogeneous hyperbolic interface of mean curvature  $H$  and Gaussian curvature  $K$ . Two shape parameters can be assigned to any interface. These

\* Corresponding author. E-mail: stephen.hyde@anu.edu.au.

<sup>†</sup> Dipartimento Chimica Inorganica ed Analitica, Università di Cagliari.

<sup>‡</sup> Infineon Ventures GmbH.

<sup>§</sup> Dipartimento Scienze Chimiche, CSGI-Università di Cagliari.

<sup>||</sup> Australian National University.

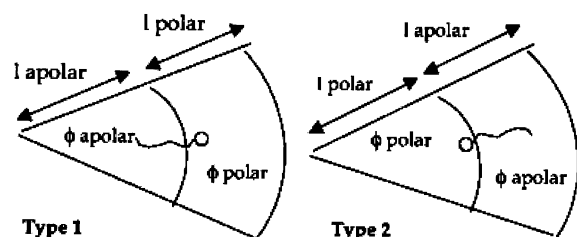


**Figure 2.** Cartoon view of a typical section through (left) type 1 and (right) type 2 surfactant mesophases, with surfactant molecules symbolized by a polar headgroup (small disks) and a single oily chain (serpentine lines). The monolayer interface, denoted by dotted arcs, cleaves the polar from the apolar domains. Domains closest to the center of curvature (the apex of the sector) describe the inner volumes. The midlayer of the bilayer is marked by dashed arcs.

are the “inner” shape parameter

$$s_{\text{in}} = \frac{v_{\text{in}}}{al_{\text{in}}} = 1 - Hl_{\text{in}} + \frac{Kl_{\text{in}}^2}{3} \quad (1a)$$

and the “outer” shape parameter

$$s_{\text{out}} = \frac{v_{\text{out}}}{al_{\text{out}}} = 1 + Hl_{\text{out}} + \frac{Kl_{\text{out}}^2}{3} \quad (1b)$$

$s_{\text{in}}$  and  $s_{\text{out}}$  describe the form of the subvolumes on either side of the interface.

In surfactant/water/oil mixtures with strongly immiscible moieties, we can define an apolar domain, which includes surfactant chains and oil, and a polar domain, which includes polar portions of the surfactant molecule and water. In what we term a type 1 system,  $s_{\text{in}}$  describes the apolar domain ( $l_{\text{in}} = l_{\text{apolar}}$ ,  $v_{\text{in}} = v_{\text{apolar}}$ ), and  $s_{\text{out}}$  describes the polar domain ( $l_{\text{out}} = l_{\text{polar}}$ ,  $v_{\text{out}} = v_{\text{polar}}$ ). For a type 2 system, this is reversed (Figures 1 and 2). The DDAB/water/tetradecane system is type 2 because of the relatively bulky double-chained surfactant apolar moiety.

The DOC cylinders model assumes that  $s_{\text{out}}$  is fixed independently of the s/w/o ratio in the microemulsion.  $H$  and  $K$  are calculated for the model as a function of connectivity  $z$  using eqs 1a and 1b. The resulting mesostructural evolution so predicted fits well the data for the DDAB/water/oil microemulsions, including small-angle X-ray scattering (SAXS) spectra,<sup>12,24,28</sup> electrical conductivity,<sup>21</sup> NMR self-diffusion coefficients,<sup>22</sup> and phase diagram data.<sup>24</sup> But that consistency between the DOC cylinders model and observations holds only in cases where the alkane species is decane or lighter.

Longer-chain alkanes lead to distinctly different mesostructures. That is apparent at once from electrical conductivity and NMR diffusion measurements<sup>10</sup> that differ from those with lower-molecular-weight alkanes. Given the reduced uptake of longer-chain oils between DDAB chains, we expect the membrane curvature to be lower. The differences are not unexpected. Indeed, as general rule,<sup>4</sup> if the oil has a chain length shorter than the surfactant tail length then oil uptake occurs. When the oil chain length exceeds the surfactant chain length no penetration occurs.

The microemulsion in the DDAB/W/tetradecane system does not extend to the oil corner.<sup>10,20</sup> This suggests that the formation of reverse spherical micelles ( $z = 0$ ) is suppressed.<sup>20</sup> Furthermore, the microemulsion phase boundary almost adjoins the bicontinuous cubic-phase regions. This suggests that at compositions close to the cubic-phase regions the microstructure must at least be reminiscent of the cubic phase, viz., a surfactant

bilayer.<sup>20</sup> Blum et al.<sup>10</sup> suggested that the tetradecane system probably always retains a bicontinuous structure. A subsequent analysis concluded that the mesostructure in the DDAB/W/tetradecane microemulsion could in fact be modeled by a disordered oil–water surfactant bilayer ( $L_3$  phase) throughout the entire microemulsion region of the phase diagram.<sup>13</sup> The “DOC lamellar” model<sup>13</sup> consists of a random bilayer lining of (or a subset of) the walls of the Voronoi domains generated as in the DOC cylinders model described above.

Although this seems plausible, there were some inconsistencies in the DOC lamellar model.<sup>13</sup> In all other known occurrences of the  $L_3$  phase, it is found to be very narrow in one direction, extending essentially as a line in a 2D phase diagram.<sup>29</sup> In the tetradecane system, the phase occupies an area rather than a line. The striking narrowness of the  $L_3$  phase is a characteristic feature associated with the constraint that the mean curvature of the two monolayers is close to the spontaneous curvature value.<sup>29</sup> Significantly, NMR measurements<sup>20</sup> have indicated that there is a substantial mesostructural evolution along some oil dilution lines. Some samples of the single-phase microemulsion region exhibit NMR self-diffusion and relaxation values close to those measured in the adjacent bicontinuous cubic phase. However, other samples show values close those measured for shorter-chain microemulsions, where the mesostructure can certainly be associated with a monolayer. This peculiar ambiguity, monolayers for some compositions and bilayers for others, has prompted us to revisit this problem.

## 2. Experimental Section

**2.1. Materials.** Didodecyl-dimethylammonium bromide (DDAB) was from Fluka and was used as received. Few samples prepared with recrystallized DDAB (from ethyl acetate) did not show appreciable differences in phase behavior. *n*-Tetradecane was from Sigma and was used as received.

**2.2. Sample Preparation.** Microemulsion samples for NMR measurements were prepared by weighing the components and were homogenized by gentle mixing. Samples of the liquid-crystal phases were prepared by weighing the components into glass tubes or ampules that were centrifuged, frozen for 12 h, flame sealed, and homogenized by cycles of storing at 60 °C and centrifuging back and forth.

Before any measurements were performed, the samples were stored at 25 °C for at least 12 days. At least two samples were made up for every composition to ensure reproducibility.

**2.3. Methods.** <sup>14</sup>N NMR measurements were performed by a Varian VXR-300 (7.05 T) spectrometer at an operating frequency of 21.67 MHz. A standard variable-temperature control unit, with an accuracy of ±0.5 °C, was used.

The <sup>14</sup>N NMR spin–lattice relaxation experiments were performed by means of the usual inversion recovery pulse sequence (PD-180°-τ-90°-AC). The spin–lattice relaxation rates,  $R_1$  were obtained by a three-parameter nonlinear fit of the partially relaxed NMR signal intensities obtained at 10 to 14 different  $\tau$  values:

$$I(\tau) = A - Be^{(-\tau R_1)} \quad (2)$$

The error in the value of  $R_1$  obtained from the fitting procedure is generally lower than ±2%.

The spin–spin relaxation rates  $R_2$  were deduced from <sup>14</sup>N NMR spectra recorded with a 90° pulse angle.  $R_2$  values were calculated from the bandwidths taken at half-height,  $\Delta\nu_{1/2}$ .

SAXS measurements were performed using both a Kiessig-geometry apparatus (point source with pinhole optics) and a home-built apparatus with Luzzati–Guinier optics using a line-shaped source. Cubic-phase spectra were collected with the Kiessig camera; microemulsion measurements were made using both cameras. All of the microemulsion scattering data presented here were collected with the Guinier camera.

The sample-to-film distance in the Kiessig apparatus was fixed at 398 mm. Some preliminary measurements were performed at  $\sim 200$  mm. The camera was coupled to an X-ray Philips generator 1120/00 with a  $^{60}\text{Co}$  ( $K\alpha$  line with  $\lambda = 1.179285 \text{ \AA}$ ) fine-focus high-intensity source (PW2216/20) using an iron filter, running typically at 25 mA, 30 KV. The beam spot at the sample plane typically had a 0.5-mm radius. The Kiessig sample chamber and flight path were evacuated to minimize parasitic scattering. The sample temperature was maintained at  $25^\circ\text{C}$  with circulating water flowing through a brass cassette in thermal contact with the sample. The temperature of the water was fixed by circulation through a Haake water bath, and the sample temperature was monitored with a thermocouple located adjacent to the sample capillary (typical thermal stability was  $\pm 0.5^\circ\text{C}$ ).

The Luzzati–Guinier camera used a system of horizontal and vertical slits that collimated and regulated the width of the primary beam. This resulted in a vertical beam profile incident on the sample with a line-shaped cross section, typically  $8 \times 1 \mu\text{m}^2$ . The monochromator was an  $8^\circ$  offcut bent quartz crystal (purchased from Inel, France); the vertical slits located after the monochromator also blocked parasitic scattering from the quartz. The camera was coupled to an X-ray Inel generator XRG 2500 operating at 2.3 kW with a Cu ( $K\alpha$  line with  $\lambda = 1.54439 \text{ \AA}$ ) long fine-focus high-intensity source (PW 2273/20) typically running at 35 mA, 35 KV. A pump created a vacuum in the camera to avoid passive scattering. The flight-path (sample-to-detector) length was continuously adjustable. To calibrate it, a thin reference sample of PTFE (Teflon) was located adjacent to the capillary. The SAXS spectrum of PTFE is well known, with a single broad scattering peak at  $\sim 30 \text{ \AA}^{-1}$  allowing the back-calculation of the sample-to-detector distance. The experiments with the Guinier camera were performed in a temperature-controlled room maintained at  $T = 25.0 \pm 0.5^\circ\text{C}$ .

All samples were injected into 80-mm thin-walled ( $1/100 \text{ mm}$ ) X-ray transparent capillaries of 0.7-mm internal diameter (W. Müller, Schönwalde, Germany), which were flame sealed prior to scattering measurements.

SAXS spectra from both cameras were recorded on photographic films (Kodak DEF 5 and DEF 354) that simultaneously recorded small- and wide-angle spectra with variable exposures between 6 and 24 h. The developed films were scanned at 800-dpi resolution and 12-bit intensity discrimination in an Alfa Arcus scanner.  $I(q)$  versus  $q$  plots were generated using NIH image software (version 2.1) that allowed radical averaging for the point-geometry Kiessig camera and vertical averaging for the linear-geometry Guinier camera.

Scattering data were processed to include the wide-angle paraffin chain characteristic spacing ( $q = 4.5 \text{ \AA}^{-1}$ ) to determine whether samples were maintained above their chain melting temperature. This is evidenced by a broad peak around  $4.2 \text{ \AA}^{-1}$ . SAXS spectra for a small selection of microemulsion samples, with intense scattering at particularly low angles, were also collected by a Guinier optics camera at Kyoto University to confirm the accuracy and efficiency of our home-built assembly Guinier camera. All spectra were processed to remove background contributions by subtracting the scattering measured from

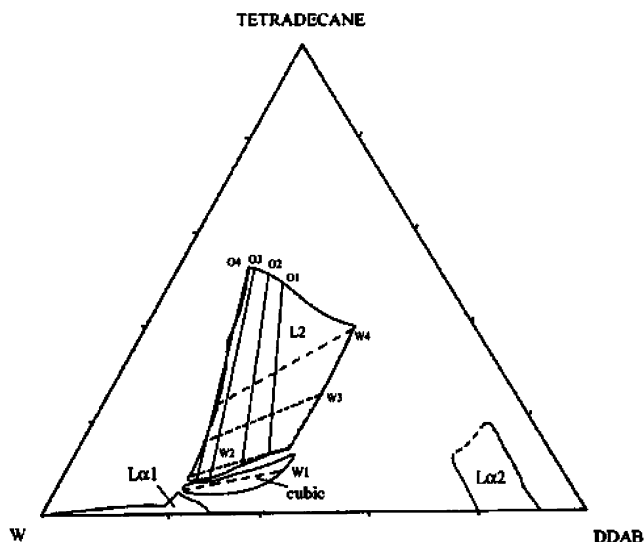


**Figure 3.** Partial DDAB/W/tetradecane phase diagram redrawn from ref 20, showing the single-phase microemulsion region (L2), the bicontinuous cubic phase, and the pair of lamellar phases ( $L\alpha 1$  and  $L\alpha 2$ ). The investigated water dilution lines (W1–W4) and oil dilution lines (O1–O4) are shown.

an empty capillary. No desmearing or other corrections were used. In the case of microemulsion peaks, there is some uncertainty in the determination of the peak position. A reference scattering standard, tristearin, was analyzed using the same method in the Guinier apparatus to determine the uncertainty in our estimation of the reciprocal scattering vector,  $q \text{ (\AA}^{-1}\text{)}$ . We estimate that uncertainty to be less than or equal to 1%.

### 3. Results and Discussion

**3.1. DDAB/Water/Tetradecane Phase Diagram.** The phase diagram of the DDAB/water (W)/tetradecane (n-c14) system at  $20^\circ\text{C}$  is shown in Figure 3, which was adapted from ref 20. The microemulsion phase boundaries are temperature-sensitive; however, all samples prepared for this study according to the phase behavior shown in Figure 3 were found to form stable one-phase microemulsions at  $25.0 \pm 0.5^\circ\text{C}$ .

The data from Fontell et al.<sup>11</sup> were used for the limits of water solubility within the pair of lamellar phases  $L\alpha 1$  and  $L\alpha 2$  on the binary DDAB–water axis. Tetradecane solubility was determined independently in both phases. The  $L\alpha 2$  phase can dissolve an increasing amount of oil as its water content increases: the maximum tetradecane uptake is  $\sim 17 \text{ wt } \%$ . The maximum solubility of tetradecane in the  $L\alpha 1$  phase is  $\sim 3 \text{ wt } \%$ . It is worth mentioning that a very stable emulsion was systematically found in the triangle oil + water +  $L\alpha 1$ .<sup>20</sup> At low oil content, between the microemulsion phase and the binary water–surfactant axis, a region of a bicontinuous cubic phase ( $V_2$ ) that seems to consist of several cubic phases, as with other oils,<sup>2</sup> is formed.<sup>1</sup>

The ternary diagram is dominated by a large microemulsion phase,  $L_2$ , located in the center of the diagram. As noted above, the most striking feature of the tetradecane microemulsion phase region, compared to that of the shorter oil systems, is that it does not extend to the oil corner. Instead, a range of microemulsion compositions admit equilibrium with almost pure oil.

**3.2.  $^{14}\text{N}$  NMR Relaxation.** The  $^{14}\text{N}$  relaxation data are shown as the relaxation rate difference  $\Delta R = R_2 - R_1$ . The relaxation rates depend on the rate of reorientation of the surfactant molecule.<sup>30</sup> Because the surfactant is adsorbed with a preferred orientation at the polar/apolar interface, the rate of reorientation depends on the shape and geometry of the interface. Taking



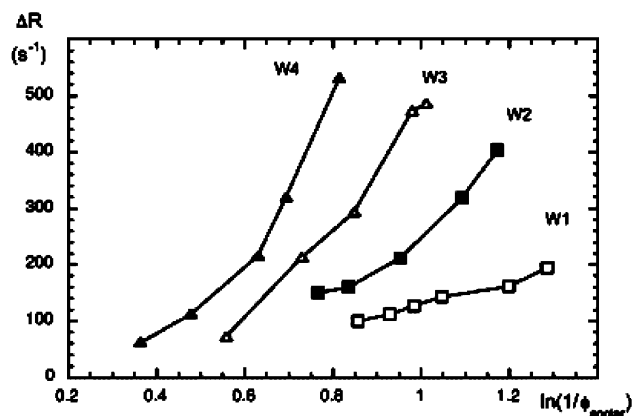


**Figure 4.**  $^{14}\text{N}$   $\Delta R$  values at  $s/o \approx 4.6$  (W1), 2.8 (W2), 1.7 (W3), and 1.06 (W4) as a function of  $\ln 1/\phi_{\text{apolar}}$  for the DDAB/W/tetradecane system.

**TABLE 1: Most Intense SAXS Peak Positions Observed within Cubic Phase Samples<sup>a</sup>**

DDAB wt %	water wt %	n-c14 wt %	$D^*$ (Å)	
W1 s/o $\approx 4.6$				
38.5	53.2	8.3	67.3	37.4
35.9	56.5	7.6	75.6	41.2
33.8	58.9	7.3	84.4	46.5
31.4	61.6	7.0	83.3	47.8
27.1	67.0	5.9	110.0	55.3
24.8	69.8	5.4	118.2	61.9

<sup>a</sup> W1 water dilution line shown in Figure 2.

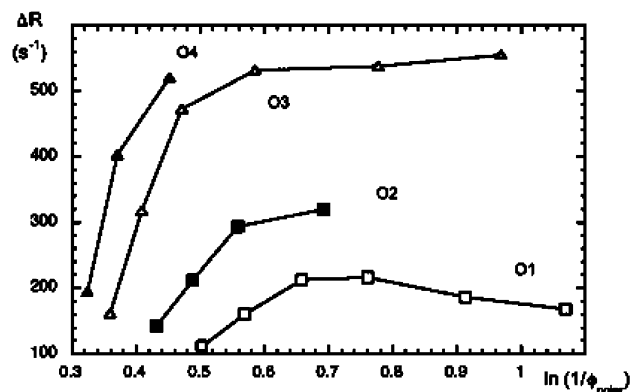


**Figure 5.**  $^{14}\text{N}$   $\Delta R$  values at  $s/w \approx 0.64$  (O1), 0.51 (O2), 0.41 (O3), and 0.36 (O4) as a function of  $\ln 1/\phi_{\text{polar}}$  for the DDAB/W/tetradecane system.

the difference, one subtracts a constant offset associated with local fast motions that are independent of the interfacial geometry,<sup>30,31</sup> leaving a dependence on slow geometry-dependent motions only. These slow motions involve lateral surfactant diffusion along the curved interface and the reorientation of the interface itself. Figure 4 shows the  $\Delta R$  values (tabulated in Table 1S) as a function of the apolar volume fraction  $\phi_{\text{apolar}} = \phi_o + 0.85\phi_s$  for samples along the water dilution lines at mass ratios  $s/o \approx 4.6$  (W1) in the bicontinuous cubic phase and  $s/o \approx 2.8$  (W2), 1.7 (W3), and 1.06 (W4) in the  $L_2$  phase. Figure 5 shows the  $\Delta R$  values (tabulated in Table 2S) as a function of the polar volume fraction  $\phi_{\text{polar}} = \phi_w + 0.15\phi_s$  for samples along the oil dilution lines at mass ratios  $s/w \approx 0.64$  (O1), 0.51 (O2), 0.40 (O3), and 0.36 (O4). The notation  $\phi_s$ ,  $\phi_w$ , and  $\phi_o$  indicates surfactant, water, and oil volume fractions, respectively. Volumes are calculated from the weight fractions assuming densities

**TABLE 2: Microemulsion SAXS Peak Positions ( $D^*$ ) along Water Dilution Lines<sup>a</sup>**

DDAB wt %	water wt %	n-c14 wt %	$D^*$ (Å)
W2 $s/o \approx 2.8$			
36.7	50.1	13.2	87
34.2	53.4	12.3	88
30.2	58.9	10.9	118
26.2	64.4	9.4	134
24.4	66.8	8.8	142
W3 $s/o \approx 1.7$			
37.9	40.0	22.1	85
31.6	49.9	18.4	109
27.9	55.9	16.2	127
24.3	61.4	14.3	150
23.4	62.8	13.8	158
W4 $s/o \approx 1.06$			
39.5	22.9	37.5	81
36.8	28.2	35.0	85
32.6	36.7	30.7	98
28.5	44.7	26.8	119
25.8	49.9	24.3	141
22.7	55.9	21.4	163

<sup>a</sup> W2, W3, and W4 in Figure 2.

of 0.998, 0.767, and 1.000  $\text{g cm}^{-3}$  for DDAB, tetradecane, and water, respectively.

The samples at the lowest oil content of the lines O1, O2, O3, and O4 belong to the bicontinuous cubic phase, the others being located in the microemulsion  $L_2$  phase.

$R_1$  was found to be essentially constant, around  $(25 \pm 5) \text{ s}^{-1}$ , and almost independent of the composition.  $R_2$  was generally much higher and concentration-dependent. When  $R_2 \gg R_1$ , we can use the approximation<sup>19,32,33</sup>

$$\Delta R = \frac{9\pi^2}{40} (\chi S)^2 J^S(0) \quad (3)$$

where  $\chi$  is the quadrupolar coupling constant,  $S$  is the order parameter, and  $J^S(0)$  is the zero-frequency spectral density of the slow motion. Because  $J^S(0)$  corresponds to the integral over the time correlation function, it can be interpreted in terms of an effective correlation time,  $J^S(0) = 2\tau_{\text{eff}}$ . The absolute product  $|\chi S|$  was obtained from quadrupolar splittings in the lamellar phase:

$$\Delta\nu_{\text{lam}} = \frac{3}{4} |\chi S| \quad (4)$$

We have measured a  $\Delta\nu_{\text{lam}}$  of 9 kHz for DDAB/W/n-c14 = 29.4/68.6/2.0. This allowed an estimate of  $\tau_{\text{eff}}$  from the  $\Delta R$  values in the microemulsion using  $\tau_{\text{eff}} \approx 5\Delta R / (2\pi\Delta\nu_{\text{lam}})^2 \approx A\Delta R$ , with  $A = 5(2\pi\Delta\nu_{\text{lam}})^2 = 1.56 \times 10^{-9} \text{ s}^2$ .  $\Delta R$  values were generally in the range of 100–600  $\text{s}^{-1}$ , corresponding to  $\tau_{\text{eff}}$  values in the range of 0.2–1  $\mu\text{s}$ .

In both Figures 4 and 5, we note that the smallest variations of  $\Delta R$ s, about 100  $\text{s}^{-1}$ , are observed at low oil content (i.e., in the cubic phase) and at low water content (i.e., at  $s/w \approx 0.64$ ). By contrast, the highest variations are found at high solvent (oil or water) content.

Consider first the water dilution line W1 inside the cubic phase. Variations of  $\Delta R$  around 100  $\text{s}^{-1}$  and then of the effective correlation time  $\tau_{\text{eff}}$  are not very large. However, they are still significant and imply that the dimensions of the domain, over which the DDAB molecule can move, change. On the basis of previous results<sup>20</sup> for ternary DDAB microemulsions formed with *n*-decane and *n*-dodecane oils, we have observed that  $\Delta R$

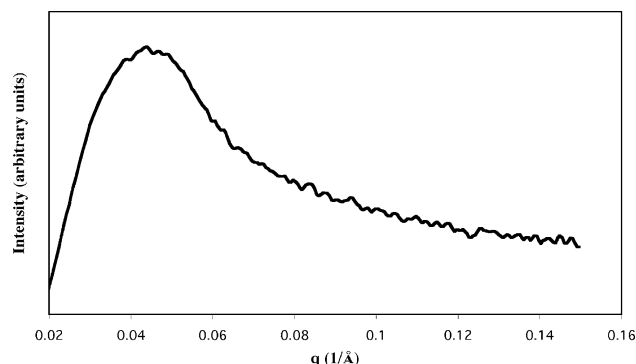


**Figure 6.** Typical small-angle X-ray scattering pattern for microemulsion samples, exhibiting a single broad peak.

$\approx 100 \text{ s}^{-1}$  is consistent with either a surfactant bilayer ordered in a bicontinuous cubic structure at low oil content or a surfactant monolayer in a water-in-oil spherical droplet at high oil content. Water self-diffusion coefficients and conductivity values allowed us to distinguish between the two types of microstructures that share this common feature of a high level of isotropic order. In the case of the oil dilution line investigated for the toluene system,<sup>9</sup>  $\Delta R$  values much lower than  $100 \text{ s}^{-1}$  were measured over the whole microemulsion region except at high volume fractions of the dispersed phase. There the system showed a clear percolation threshold in the proximity of the boundary with the lamellar phase. Indeed, on the basis of conductivity and NMR relaxation data, no spherical w/o droplets appear to occur at any composition for this toluene system. Here the  $^{14}\text{N}$  NMR relaxation rates were also measured in the lamellar  $L_{\alpha 2}$  phase, and  $\Delta R$  values in the range of  $400\text{--}1200 \text{ s}^{-1}$  were found. However,  $\Delta R$  values in the range of  $400\text{--}600 \text{ s}^{-1}$  were found in the  $L_2$  region at low oil content in the proximity of the phase boundary with the bicontinuous cubic phase for decane and dodecane oils.<sup>20</sup> It is worth mentioning that  $^{14}\text{N}$  NMR quadrupolar relaxation has been proven to be a new powerful and reliable approach at the molecular level to investigate microstructural transitions and percolation phenomena in DDAB microemulsions.<sup>34</sup>

Qualitatively,  $\Delta R$  values around  $100 \text{ s}^{-1}$  are indicative either of isotropic long-range-ordered bilayers or of almost monodisperse w/o droplets stabilized by a surfactant monolayer. In the latter case, interdroplet interactions also should be rather low in order to retain an isotropic long-range pseudo-order. By comparison,  $\Delta R$  values exceeding  $500 \text{ s}^{-1}$  indicate high levels of anisotropic arrangements and/or interactions such as in the lamellar phase, in concentrated bicontinuous microemulsions, and in polydisperse aggregates. If anisotropic interactions dominate, then  $\Delta R$  values increase significantly and independently of the bilayer or monolayer organization.

What is then suggested by these arguments is that all  $\Delta R$  values in the range of  $100\text{--}500 \text{ s}^{-1}$  indicate transition states that are characterized by strong interaggregate interactions and fluctuations of the average microstructure among different sizes and shapes.

**3.3. SAXS Results.** Two to three narrow scattering peaks were evident for samples lying within the cubic-phase region. Two peaks could be unambiguously located in  $q$  space (Table 1). Microemulsions gave rise to a single, broad scattering peak at low angle, characteristic of other DDAB microemulsions (Figure 6). Here we ignore the peak width and reduce each microemulsion SAXS spectrum to a single number, located at the  $q$  value that corresponds to the local maximum scattering intensity. The shape of the microemulsion scattering peaks

**TABLE 3: Microemulsion SAXS Peak Positions ( $D^*$ ) along the Oil Dilution Lines<sup>a</sup>**

DDAB wt %	water wt %	n-c14 wt %	$D^*$ (Å)
O1 s/w $\approx 0.64$			
31.6	49.9	18.4	109
28.5	44.7	26.8	119
26.5	40.2	33.3	140
23.2	35.2	41.6	148
O2 s/w $\approx 0.51$			
30.2	58.9	10.9	118
28.0	55.8	16.2	127
25.7	49.9	24.4	141
O3 s/w $\approx 0.41$			
26.2	64.4	9.4	134
24.3	61.5	14.2	150
22.7	55.9	21.4	163
19.9	47.5	32.5	192
16.8	40.4	42.8	240
O4 s/w $\approx 0.36$			
24.4	66.8	8.8	142
23.4	62.8	13.8	158

<sup>a</sup> O1–O4 in Figure 2.

(typically broad and slightly asymmetric) led to a “nominal” imprecision of 5–10% in the location in  $q$  space of the scattering maximum. This uncertainty affected the final conclusions that rely on logarithmic variations of  $q$  values very little. The results are collected in Tables 2 and 3.

**3.4. Monolayer–Bilayer Models.** Swelling laws of amphiphilic mesostructures have been derived and related to the shape parameters in a number of papers.<sup>27,35–38</sup>

Those relations allow us to go beyond the numerics of DOC models and analyze mesostructures more generally. The analytic swelling laws result from a significant, but chemically relevant, mathematical assumption: they demand that the mesostructure at the apolar/polar interface be “homogeneous” (i.e., close to constant interfacial curvatures throughout the sample). That approximation translates chemically to a requirement that the amphiphile is chemically monodisperse and leads to reasonably stiff membranes. Then molecular packing within the membrane, set by a fixed surfactant parameter, accommodates only small inhomogeneities in curvature. This assumption seems to be particularly suitable for DDAB mixtures, presumably because of the effectively rigid average molecular conformation taken up by the surfactant molecule.

NMR data, together with the ternary phase diagram, suggest that the ternary tetradecane microemulsion consists of a hyperbolic bilayer at low oil content and a hyperbolic monolayer at higher oil content. Because the adjoining cubic phase is type 2, we can also confidently assume that the microemulsion structure is type 2.

Assuming homogeneity and swelling at a constant shape parameter, the following ideal relations apply to a hyperbolic bilayer<sup>35</sup>

$$\left(\frac{l_{\text{in}}}{R}\right) \approx \phi_{\text{in}}^{s_{\text{in}}} \quad \text{or} \quad \left(\frac{2l_{\text{in}}}{D^*}\right) \approx \phi_{\text{in}}^{s_{\text{in}}} \quad (5)$$

For a type 2 structure,  $l_{\text{in}}$  is the polar thickness  $l_{\text{polar}}$ ,  $s_{\text{in}}$  is the inner (polar) shape parameter,  $D^*$  is the characteristic (pseudo-Bragg) correlation distance in the aggregate (the scattered peak), and  $\phi_{\text{in}}$  is the polar volume fraction.

A local picture of hyperbolic bilayers is shown in Figure 7. Evidently, the repeat spacing detected in the SAXS spectra,  $D^*$ , must scale linearly with  $2R$ , twice the radius of curvature of

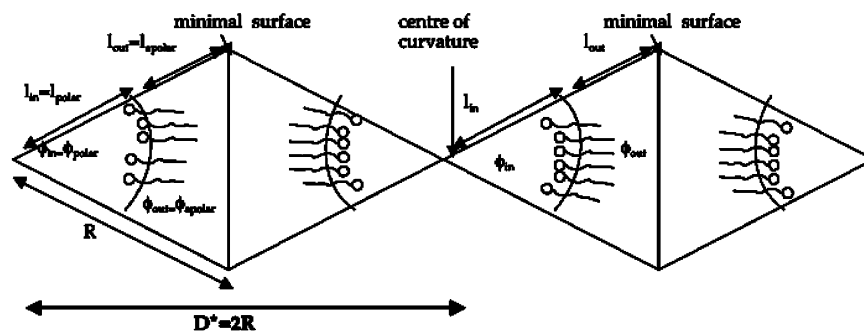


Figure 7. Schematic cross section through a hyperbolic bilayer (type 2).

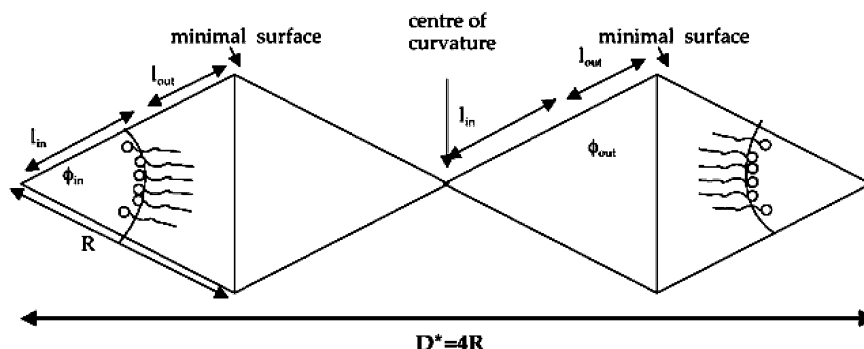


Figure 8. Schematic cross section through a hyperbolic monolayer (type 2).

the minimal surface. Here we assume for convenience that  $D^*$  is the smallest repeat distance in the structure. The scaling analysis is in any case insensitive to that assumption.

In a type 2 structure, the centers of curvatures on either side of the apolar interfaces lie within the polar domains, and the bilayer lies on either side of the central dividing minimal surface that lies midway between both centers of curvature. Besides, the apolar shape parameter ( $s_{out}$ ) is larger than the polar one ( $s_{in}$ );  $s_{out}$  is generally greater than unity, but  $s_{in}$  is always smaller than unity.

Consider now a monolayer. First, the meaning of monolayer versus bilayer has to be clarified. In fact, the distinction is artificial because any bilayer can be decomposed into a pair of monolayers and vice versa. For our analysis, a more useful definition is needed. We define the structure as a bilayer structure if the bilayer has constant thickness. In other words, where a pair of monolayers are parallel, we refer to the mesostructure as a bilayer structure. Otherwise, it is described as a monolayer. Note that the definition is consistent with Figure 7. The pair of monolayers are displaced at a distance of  $2l_{out}$  toward both sides of the central dividing (minimal) surface.

The topological form of a single-sheeted hyperbolic bilayer is quite different from that of a monolayer. In that case, the bilayer winds through space, carving out a pair of entangled, but discrete, polar domains, separated by an apolar film as in bicontinuous cubic phases. In contrast, a single-sheeted hyperbolic monolayer generates a pair of interwoven, discrete labyrinths. One is polar; the other, apolar. The analogue of Figure 7 for the monolayer case is illustrated in Figure 8.

Here the polar volume fraction  $\phi_{in}$  is

$$\phi_{in} \approx \frac{1}{2} \left( \frac{l_{in}}{R} \right)^{1/s_{in}} \quad (6)$$

and the repeat spacing is twice that of the bilayer case,

$$\phi_{in} \approx \frac{1}{2} \left( \frac{4l_{in}}{D^*} \right)^{1/s_{in}} \quad (7)$$

or

$$\left( \frac{2l_{in}}{D^*} \right) \approx (2\phi_{in})^{s_{in}} \quad (8)$$

or

$$\left( \frac{l_{in}}{D^*} \right) \approx 2^{s_{in}-1} \phi_{in}^{s_{in}} \quad (9)$$

Now, a comparison of eqs 5 and 9 suggest the following generalization (removing the common multiple of 2):

$$\left( \frac{l_{in}}{D^*} \right) \approx f^{s_{in}-1} \phi_{in}^{s_{in}} \quad (10)$$

where

$$f \in [1, 2] \quad (11)$$

viz.,  $f = 1$  for the bilayer- and  $f = 2$  for the monolayer-limit cases.

**3.5. Modeling of Microstructural Transitions along Oil Dilution Lines.** Let us assume first that either a bilayer or a monolayer arrangement along each oil dilution path O1–O4 is retained.

The thickness of a polar domain ( $l_{polar} = l_{in}$ ) on oil dilution can be assumed to be constant. So from eq 10, a (natural logarithmic) log–log plot of  $D^*$  vs  $1/\phi_{polar}$  along each oil dilution path O1–O4 should be linear with a local gradient of  $s_{in}$ , regardless of the mesostructural class (monolayer or bilayer). The plots are shown in Figure 9; in all cases, ln–ln plots are roughly linear over the entire range of the data. However, in all cases the slopes exceed unity, giving an unphysical value of  $s_{in}$  (that must be less than unity). The data are inconsistent with

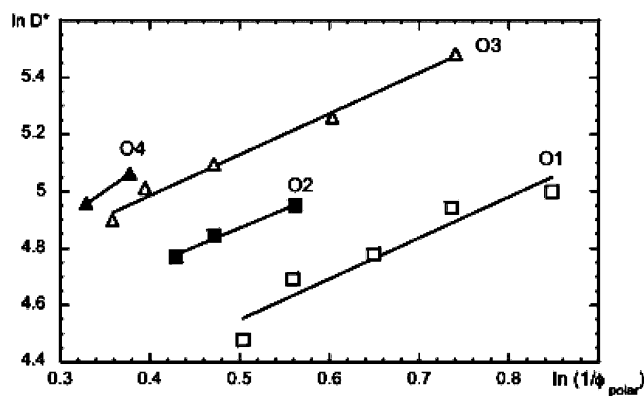


**Figure 9.** Experimental  $\ln D^*$  at  $s/w \approx 0.64$ (O1),  $0.51$ (O2),  $0.41$ -(O3), and  $0.36$ (O4) as a function of  $\ln 1/\phi_{\text{polar}}$  for the DDAB/W/tetradecane system. All slopes are greater than unity.

the hypothesis that the mesostructure remains either a bilayer or a monolayer along the oil dilution lines. The apparent linear dependence thus masks a more complex functional form, which we seek to model.

The swelling plots reveal a highly unusual situation: linear dimensions within the microemulsion grow more rapidly than accompanying volume changes. This inflationary behavior is curious and points at once to novel microstructural variation within the microemulsion. Indeed, this swelling is incompatible with standard structural models that suppose the retention of bilayer or monolayer character on swelling. However, the behavior is in agreement with the hypothesis of a bilayer–monolayer transition along the oil dilution lines.

The bilayer–monolayer transition<sup>39,40</sup> may be pictured as an inflation of the bilayers. First, the pair of disconnected polar domains are linked via bilayer punctures or bridges fusing adjacent (parallel) monolayers. The single, connected monolayer is then relaxed to give monolayers of uniform curvature and apolar domains with a uniform shape parameter. Intermediate stages of this process are illustrated in Figure 10. The inflation process swells the entire mesostructure, and characteristic distances within the structure increase more rapidly than they could in the absence of such a transition. Characteristic lengths in the monolayer are double those of the bilayer with identical  $s_{\text{in}}$  at a fixed volume fraction.

We can now compare our experimental data with the swelling relation (eq 10). Two unknowns remain: the magnitude of the preferred inner shape parameter,  $s_{\text{in}}$ , and the functional form of  $f(\phi_{\text{in}})$  that describes the rate of evolution from a bilayer to a monolayer upon oil addition.

NMR data presented elsewhere<sup>20</sup> suggested that the microemulsion structure near the microemulsion–cubic phase transition is similar to that in the cubic phase. We can estimate the values of  $s_{\text{in}}$  and  $s_{\text{out}}$  from the cubic-phase volume fractions by the following relations. These hold exactly for an ideal sponge but are good approximations for bicontinuous cubic mesophases:<sup>38</sup>

$$s_{\text{out}} = \frac{3 - (\cos(\Delta\phi_{\text{out}}) - 3^{1/2} \sin(\Delta\phi_{\text{out}}))^2}{3 - 3(\cos(\Delta\phi_{\text{out}}) - 3^{1/2} \sin(\Delta\phi_{\text{out}}))^2} \quad (12)$$

where

$$\phi_{\text{out}} = \phi_{\text{apolar}} \text{ and } \Delta\phi_{\text{out}} = \frac{1}{3} \cos^{-1} \left( \frac{4h\phi_{\text{out}}}{3} \right) \text{ with } h = \frac{3}{4} \quad (13)$$

and<sup>27</sup>

$$s_{\text{in}} = \frac{9s_{\text{out}} - 4}{9(2s_{\text{out}} - 1)} \quad (14)$$

We apply eqs 12 and 13 to compositions lying within the cubic-phase region of the phase diagram (i.e., on dilution line W1 shown in Figure 3) to deduce values of  $s_{\text{out}}$  between 1.02 and 1.05. Equation 14 allows for the estimation of the inner shape parameter from those values and reveals it to remain fixed for all compositions on water dilution line W1 (i.e.,  $s_{\text{in}} = 0.55$ ). Consistent with that calculation, a constant value of  $s_{\text{in}}$  for all oil dilution paths within the microemulsion region (O1–O4) is assumed. Samples within a single dilution series are expected to have fixed value of  $s_{\text{in}}$ , consistent with expectations for type 2 mesophase samples with various oil content and the same polar content (whose inner shape, characterized by  $s_{\text{in}}$ , is set only by the polar solvent and counterions and is unlikely to vary significantly except at very low hydration). We next adopt the simplest numerical hypothesis describing the bilayer–monolayer transition: along oil dilution paths O1–O4, the mesostructures evolve linearly with changing volume fractions from a bilayer ( $f = 1$ ) at the lowest oil content to a monolayer ( $f = 2$ ) at the highest oil content. Assume for now that the function  $f = f(\phi_{\text{in}})$  is linear and that the functional form of  $f$  is calculated according to  $f = 1$  (bilayer) for the highest value of  $\phi_{\text{in}} = \phi_{\text{polar}}$  (or lowest oil content) and  $f = 2$  (monolayer) for the lowest value of  $\phi_{\text{in}}$  (highest oil content). The resulting equations describing the form of  $f(\phi_{\text{in}})$  are listed in Supporting Information.

These functional forms are introduced in eq 10 along with the estimated value of  $s_{\text{in}}$ , allowing new estimates of the dependence of the characteristic length in the microemulsion ( $D^*$ ) on oil content (parametrized by  $1/\phi_{\text{in}} = 1/\phi_{\text{polar}}$ ) within the assumptions of our punctured bilayer–monolayer model.  $\ln$ – $\ln$  plots of the expected scaling of characteristic distances in the microemulsion with composition are shown in Figure 11 together with the experimental data ( $\ln(D^*/x)$  versus  $\ln(1/\phi_{\text{polar}})$ ). The fit between experiment and theory involves a single adjustable parameter  $x$ . That parameter is the polar thickness ( $l_{\text{in}}$ , see eq 10), which determines the intercept of the experimental scaling plot. Fit values are displayed in Figure 11. The corresponding expected trends assuming that the microemulsion remains (i) a bilayer (lower dashed line) and (ii) a monolayer (upper dashed line) throughout the oil dilution series are also shown.

The agreement between the experimentally determined variation in the scattering peak position ( $D^*$ ) with oil content and that predicted by our simple bilayer–monolayer (linear  $f(\phi_{\text{in}})$ ) model is good, with physically reasonable values of fit parameter  $x$ . Evidently, there is no need to assume a more complex structural transition rate than a linear one with oil concentration. The theory also allows for the determination of the outer shape parameter ( $s_{\text{out}}$ ), in reasonable agreement with the value expected from theory given the rather sparse data (Table 4).

In summary, the SAXS data cannot be reconciled with a microemulsion mesostructure based exclusively on a monolayer or bilayer model. The inflated swelling of characteristic lengths in the microemulsion samples with oil dilution is rather compatible with a gradual and smooth transition from random hyperbolic bilayers (similar to that proposed in the earlier DOC lamellar model<sup>13</sup>) on the low-oil side of the single-phase microemulsion region in the ternary phase diagram to a random hyperbolic monolayer (DOC cylinder model<sup>12,24–26,28</sup>) at the higher-oil boundary.



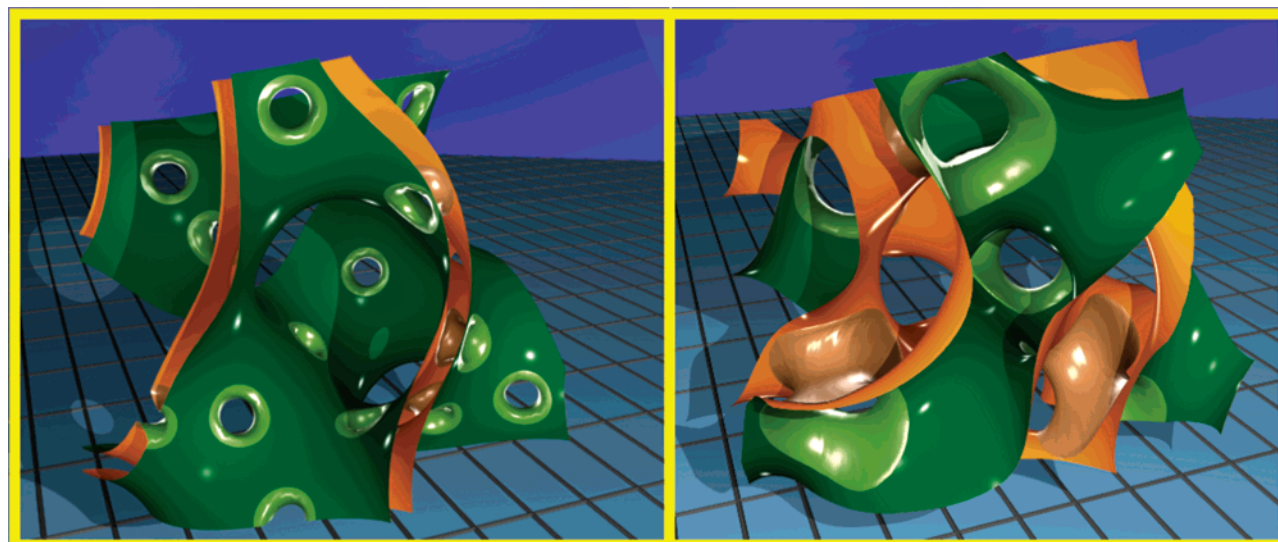


**Figure 10.** Computer renditions of intermediate stages during the bilayer–monolayer transition. The left-hand image shows a pair of parallel monolayers, with some bridging material linking the monolayers (light-green areas). The volume bounded by the orange surfaces is the inner volume, which contains the apolar material in a type 2 mesophase. This can be described as a defective (punctured) bilayer phase. The right-hand image shows a topologically similar structure to the previous one, though the density of the bridges is lower. The structure has relaxed to adopt a uniform shape throughout the inner (apolar) volume; it is best described as a type 2 (bicontinuous) monolayer phase.

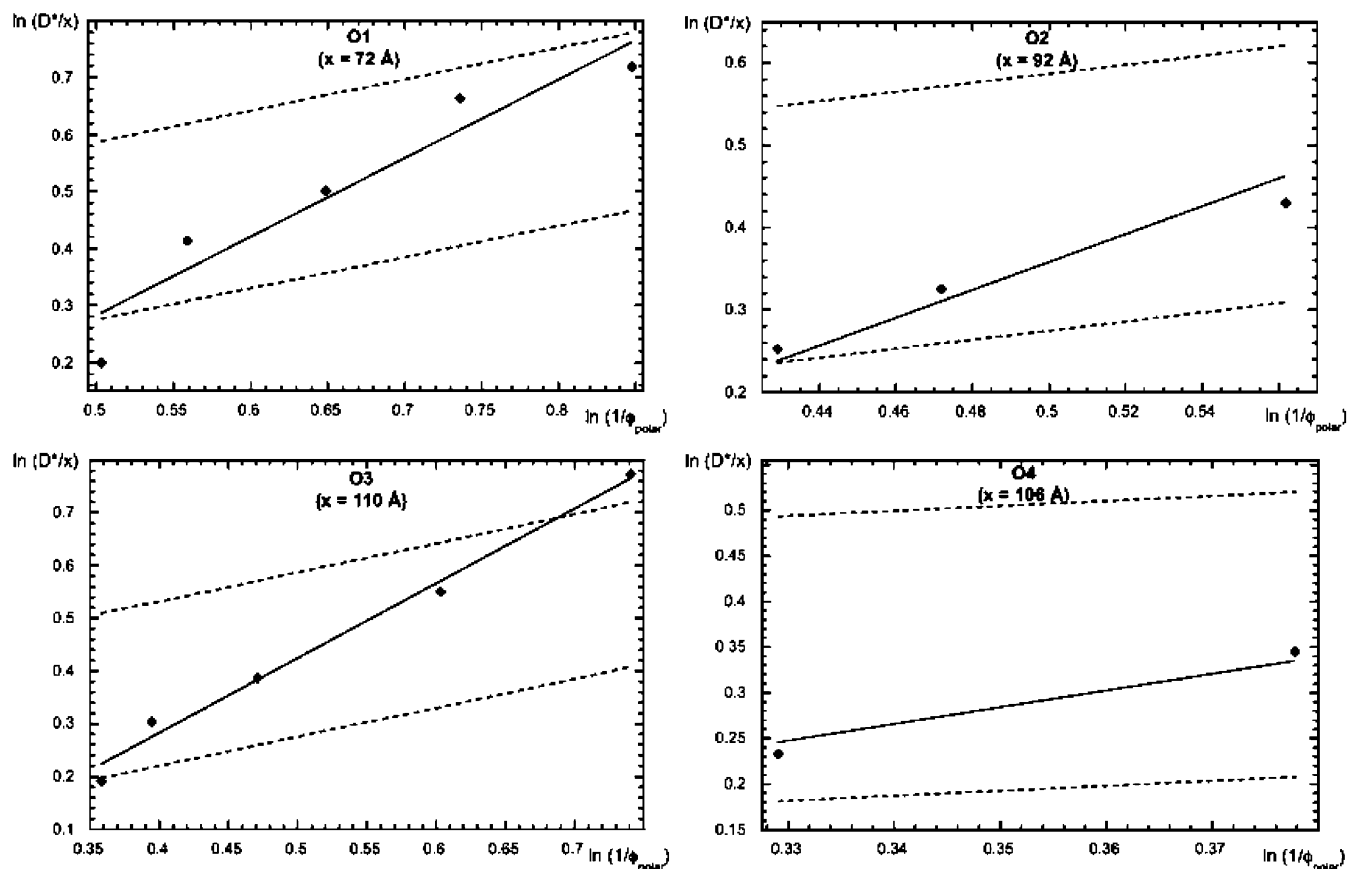


**Figure 11.** Swelling of characteristic distance  $D^*$  in microemulsions as a function of polar volume fractions  $\phi_{\text{polar}}$  ( $\ln D^*_{\text{theor}}$  vs  $\ln 1/\phi_{\text{polar}}$ ) for oil dilution paths O1–O4. The linear fits give the approximate (theoretical) power-law swelling exponents (Table 4). Theoretical trends for a monolayer and a bilayer are also shown (upper and lower dashed lines, respectively). The single fit parameter  $x$ , the thickness of the polar layer, is adjusted to best match theory and data.

#### 4. Conclusions

Mesostructural features of the DDAB/W/tetradecane microemulsion have been reinvestigated by  $^{14}\text{N}$  NMR relaxation and SAXS measurements. The modeling of SAXS data on the basis of a gradual bilayer–monolayer transition along oil dilution lines leads, we believe, to a convincing conclusion that is consistent

with the NMR measurements. Type 2 bilayers, characterized by closely spaced, parallel monolayers (cleaving the volume into a pair of disjointed polar subvolumes), are formed in single-phase microemulsions at lower oil content. The bilayers evolve into (type 2) monolayers (containing a single polar and a complementary single apolar volume) at higher oil content. The



**TABLE 4: Experimental vs Theoretical Swelling Exponents for Oil Dilution Lines O1–O3<sup>a</sup>**

dilution lines	exptl exponent	theor exponent
O1	1.44	1.38
O2	1.31	1.40
O3	1.43	1.42

<sup>a</sup> O4 contains insufficient data to admit a meaningful fit. The theoretical exponents are calculated assuming an inner shape parameter of 0.55 for all compositions and linear evolution with volume fraction from bilayers to monolayers on oil dilution. The exponents reflect the approximately power-law scaling of characteristic lengths within the microemulsions with polar volume fraction (equal to the slopes of the plots in Figure 7).

SAXS and NMR data suggest a continuous transition between the bilayer and monolayer mesostructures, mediated by the formation and growth of punctures within the bilayers (equivalently, growth of channels linking adjacent monolayers), previously described theoretically.<sup>39</sup>

Similarly, strong variations of the mesostructure can also be suggested from NMR data along water dilution lines. The analysis of SAXS data along the water dilution lines is still in progress, and the modeling of mesostructural evolution on water dilution will be reported in a later publication.

We conclude that the experimental data that we have reported for the ternary DDAB/W/tetradecane system are all consistent with a continuous, novel, previously experimentally unknown evolution of the mesostructure within the one-phase microemulsion region, characterized by very rapid inflationary swelling of the self-assembled water- and oil-continuous mesostructure on oil dilution.

**Acknowledgment.** MIUR-PRIN (40%) (Italy) and Consorzio Sistemi Grande Interfase (CSGI-Firenze) are acknowledged for financial support. We thank Dr. H. Hasegawa and colleagues (Kyoto University) for access to their SAXS apparatus for comparative measurements. M.O. thanks the Department of Applied Mathematics ANU, Canberra, for its hospitality and support during a stay of 9 months. We also thank Gerd Schröder for computing and rendering Figure 10 using the facilities of the A.N.U. Vizlab and Tim Sawkins for his technical assistance. S.T.H. is grateful to all of his co-authors for their extreme patience in finalizing the paper.

**Supporting Information Available:** <sup>14</sup>N NMR data along the water and oil dilution lines. Derivation of *a* and *b* fit parameters. Values of *a* and *b* parameters for the linear mono/bilayer model. This material is available free of charge via the Internet at <http://pubs.acs.org>.

## References and Notes

- (1) Maddaford, P. J.; Toprakcioglu, C. *Langmuir* **1993**, *9*, 2868–2878.

- (2) Barois, P.; Hyde, S. T.; Ninham, B.; Dowling, T. *Langmuir* **1990**, *6*, 1136–1140.
- (3) Ninham, B. W.; Chen, S. J.; Evans, D. F. *J. Phys. Chem.* **1984**, *88*, 5855.
- (4) Chen, S. J.; Evans, D. F.; Ninham, B. W.; Mitchell, D. J.; Blum, F. D.; Pickup, S. *J. Phys. Chem.* **1986**, *90*, 842.
- (5) Hyde, S. T.; Andersson, S.; Larsson, K.; Blum, Z.; Landh, T.; Lidin, S.; Ninham, B. W. *The Language of Shape*; Elsevier: Amsterdam, 1997; Chapters 1–5.
- (6) Monduzzi, M.; Knackstedt, M. A.; Ninham, B. W. *J. Phys. Chem.* **1995**, *99*, 17772.
- (7) Caboi, F.; Monduzzi, M. *Prog. Colloid Polym. Sci.* **1998**, *108*, 153.
- (8) Olla, M.; Monduzzi, M.; Ambrosone, L. *Colloids Surf., A* **1999**, *160*, 23.
- (9) Olla, M.; Monduzzi, M. *Langmuir* **2000**, *16*, 6141–6147.
- (10) Blum, F. D.; Pickup, S.; Ninham, B. W.; Chen, S. J.; Evans, D. F. *J. Phys. Chem.* **1985**, *89*, 711.
- (11) Fontell, K.; Ceglie, A.; Lindman, B.; Ninham, B. W. *Acta Chem. Scand. A* **1986**, *40*, 247.
- (12) Barnes, I. S.; Hyde, S. T.; Ninham, B. W.; Derian, P.-J.; Drifford, M.; Zemb, T. N. *J. Phys. Chem.* **1988**, *92*, 2286.
- (13) Barnes, I. S.; Derian, P. J.; Hyde, S. T.; Ninham, B. W.; Zemb, T. N. *J. Phys. (Orsay, Fr.)* **1990**, *51*, 2605.
- (14) Eastoe, J. *Langmuir* **1992**, *8*, 1503.
- (15) Eastoe, J.; Heen, R. K. *J. Chem. Soc., Faraday Trans.* **1994**, *90*, 487.
- (16) Samseth, J.; Chen, S.-H.; Litster, J. D.; Huang, J. S. *J. Appl. Crystallogr.* **1988**, *21*, 835–839.
- (17) Samseth, J.; Chen, S.-H.; Litster, J. D.; Huang, J. S. In *Phase Transitions in Soft Condensed Matter*; Riste, T., Sherrington, D., Eds.; Plenum Press: New York, 1989.
- (18) Skurtveit, R.; Olsson, U. *J. Phys. Chem.* **1991**, *95*, 5353.
- (19) Skurtveit, R.; Olsson, U. *J. Phys. Chem.* **1992**, *96*, 8640.
- (20) Monduzzi, M.; Caboi, F.; Larche, F.; Olsson, U. *Langmuir* **1997**, *13*, 2184.
- (21) Knackstedt, M. A.; Ninham, B. W. *Phys. Rev. E* **1994**, *50*, 2839.
- (22) Knackstedt, M. A.; Ninham, B. W.; Monduzzi, M. *Phys. Rev. Lett.* **1995**, *75*, 653.
- (23) Israelachvili, J. N.; Mitchell, D. J.; Ninham, B. W. *J. Chem. Soc., Faraday Trans. 2* **1976**, *72*, 1525–1568.
- (24) Hyde, S. T.; Ninham, B. W.; Zemb, T. *J. Phys. Chem.* **1989**, *93*, 1464–1471.
- (25) Ninham, B. W.; Barnes, I. S.; Hyde, S. T.; Derian, P.-J.; Zemb, T. N. *Europhys. Lett.* **1987**, *4*, 561.
- (26) Barnes, I. S.; Hyde, S. T.; Derian, P.-J.; Drifford, M.; Ninham, B. W.; Zemb, T. N.; Warr, G. G. *Prog. Colloid Polym. Sci.* **1988**, *76*, 1–6.
- (27) Hyde, S. T. *Langmuir* **1997**, *13*, 842–851.
- (28) Zemb, T. N.; Hyde, S. T.; Derian, P.-J.; Barnes, I. S.; Ninham, B. W. *J. Phys. Chem.* **1987**, *91*, 3814.
- (29) Anderson, D.; Wennerström, H.; Olsson, U. *J. Phys. Chem.* **1989**, *93*, 4243–4253.
- (30) Wennerström, H.; Lindman, B.; Söderman, O.; Drakenberg, T.; Rosenholm, J. B. *J. Am. Chem. Soc.* **1979**, *101*, 6860–6864.
- (31) Halle, B.; Wennerström, H. *J. Chem. Phys.* **1981**, *75*, 1928.
- (32) Monduzzi, M.; Olsson, U.; Söderman, O. *Langmuir* **1993**, *9*, 2914.
- (33) Leaver, M. S.; Olsson, U.; Wennerström, H.; Strey, R. *J. Phys. II* **1994**, *4*, 515–531.
- (34) Monduzzi, M.; Mele, S. *J. Phys. Chem. B* **2001**, *105*, 12579–12582.
- (35) Hyde, S. T. *Colloids Surf., A* **1995**, *103*, 227–247.
- (36) Engblom, J.; Hyde, S. T. *J. Phys. II* **1995**, *5*, 171–190.
- (37) Hyde, S. T. *Curr. Opin. Solid State Mater. Sci.* **1996**, *1*, 653–662.
- (38) Hyde, S. T. In *Handbook of Applied Surface and Colloid Chemistry*; Holmberg, K., Ed.; Wiley: Chichester, U.K., 2001; Chapter 16.
- (39) Hyde, S. T. *Colloids Surf., A* **1997**, *129*, 207–225.
- (40) Hyde, S. T.; Schröder, G. *Curr. Opin. Colloid Interface Sci.* **2003**, *8*, 5–14.